

## Atomic-Ordering-Induced Quantum Phase Transition between Topological Crystalline Insulator and $Z_2$ Topological Insulator \*

Hui-Xiong Deng(邓惠雄)<sup>1,2\*\*</sup>, Zhi-Gang Song(宋志刚)<sup>1</sup>, Shu-Shen Li(李树深)<sup>1,2,3</sup>,  
Su-Huai Wei(魏苏淮)<sup>4\*\*</sup>, Jun-Wei Luo(骆军委)<sup>1,2,3\*\*</sup>

<sup>1</sup>State Key Laboratory of Superlattices and Microstructures, Institute of Semiconductors,  
Chinese Academy of Sciences, Beijing 100083

<sup>2</sup>University of Chinese Academy of Sciences, Beijing 100049

<sup>3</sup>Beijing Academy of Quantum Information Sciences, Beijing 100193

<sup>4</sup>Beijing Computational Science Research Center, Beijing 100094

(Received 21 February 2018)

*Topological phase transition in a single material usually refers to transitions between a trivial band insulator and a topological Dirac phase, and the transition may also occur between different classes of topological Dirac phases. It is a fundamental challenge to realize quantum transition between  $Z_2$  nontrivial topological insulator (TI) and topological crystalline insulator (TCI) in one material because  $Z_2$  TI and TCI have different requirements on the number of band inversions. The  $Z_2$  TIs must have an odd number of band inversions over all the time-reversal invariant momenta, whereas the newly discovered TCIs, as a distinct class of the topological Dirac materials protected by the underlying crystalline symmetry, owns an even number of band inversions. Taking PbSnTe<sub>2</sub> alloy as an example, here we demonstrate that the atomic-ordering is an effective way to tune the symmetry of the alloy so that we can electrically switch between TCI phase and  $Z_2$  TI phase in a single material. Our results suggest that the atomic-ordering provides a new platform towards the realization of reversibly switching between different topological phases to explore novel applications.*

PACS: 73.43.Nq, 71.20.Nr, 73.20.At, 71.15.Mb

DOI: 10.1088/0256-307X/35/5/057301

Topological insulators (TIs)<sup>[1–8]</sup> are an emerging class of quantum materials, which are nontrivial under the  $Z_2$  topological classification (i.e.,  $Z_2 = 1$ ) usually resulting from band inversions occurring at an odd number of time-reversal-invariant momenta (TRIMs). These materials possess topological surface states spanning the insulating bulk bandgap, when they are placed next to a vacuum or a  $Z_2$  topological trivial material, owing to the impossible change of the characterized topological invariant in crossing the interface between them without closing the band gap.<sup>[9]</sup> These spin-momentum-locked helical surface states exhibit Dirac-cone energy dispersion across the bulk bandgap, and are topologically protected by the time-reversal symmetry (TRS).<sup>[2,6,7,9]</sup> However, some materials such as SnTe also possess band inversions, whereas they are  $Z_2$  topological trivial because their band inversions occur at an even number of TRIMs (e.g., SnTe band inversions occur at 4  $L$ -points.<sup>[10,11]</sup> Recent theoretical results followed by experimental validations have suggested that these materials are topological crystalline insulators (TCIs),<sup>[12–15]</sup> a subclass of topological insulators in which the underlying crystalline symmetry replaces the role of the TRS in ensuring a new topological invariant of mirror Chern

number instead of the  $Z_2$  index.

$Z_2$  TI and TCI have very distinct topology of surface electronic structures,<sup>[16–18]</sup> despite their common characteristics of topological protected gapless spin-momentum-locked surface states and an intrinsic orbital texture switch occurring exactly at the Dirac point.<sup>[19,20]</sup> For instance, the Dirac points in  $Z_2$  TIs are nailed to TRIMs as a result of TRS protection,<sup>[4–8,21]</sup> whereas the Dirac points in TCIs are away from the TRIMs,<sup>[13–18]</sup> demonstrating their irrelevance to the TRS-related protection. As a consequence of different topological invariants, the  $Z_2$  topological states are robust against general time-reversal invariant perturbations, however, the TCI topological states have a much wider range of tunable electronic properties under various perturbations, such as structural distortion, magnetic dopant, mechanical strain, thickness engineering, and disorder. Specifically, topological surface states in the  $Z_2$  TIs are susceptible to TRS-breaking disorders such as magnetic defects; however, in the TCI system it is possible to realize magnetic yet topologically protected surface states due to its irrelevance to the TRS, which is a fundamentally distinct from the  $Z_2$  TIs. Subsequently, the magnetic and superconducting orders in

\*Supported by the Major State Basic Research Development Program of China under Grant No 2016YFB0700700, and the National Natural Science Foundation of China (NSFC) under Grants Nos 11634003, 11474273, 61121491 and U1530401. J. W. L. was also supported by the National Young 1000 Talents Plan. H. X. D. was also supported by the Youth Innovation Promotion Association of CAS (2017154).

\*\*Corresponding authors. Email: hxdeng@semi.ac.cn; suhuaiwei@csrc.ac.cn; jwluo@semi.ac.cn

© 2018 Chinese Physical Society and IOP Publishing Ltd

the TCI surface states can be disparate from those observed in the  $Z_2$  TIs. Perturbations without breaking TRS in the TCIs can move Dirac points in momentum space, mimicking the effect of a gauge field vector potential,<sup>[22]</sup> and open an energy gap at the Dirac point, generating Dirac mass.<sup>[23,24]</sup> Changing the alloying composition<sup>[25]</sup> or applying a strain<sup>[18,22]</sup> are two recently demonstrated effective ways of moving surface Dirac points in TCIs. Moreover, accompanying the formation of offspring Dirac cones, both Lifshitz transitions and Van Hove singularity (VHS) were aware of the existing in TCI band structures.<sup>[20,23]</sup> Considering the broad applications of magnetic materials in modern electronics, such topologically protected surface states compatible with magnetism will be of considerable interest regarding integrating TI materials into future electronic devices. *Because  $Z_2$  TI and TCI topological states have their own unique topological features, the feasibility of reversible topological phase transition between  $Z_2$  TI and TCI phases in a single material is highly desirable to explore novel applications.*

Although some attempts have been made to achieve such topological phase transition by reducing the crystal lattice symmetry through strain engineering or forming surfaces,<sup>[10,11]</sup> to the best of our knowledge, it has not been realized either in theoretical predictions or experimental observations. For instance, Fu *et al.*<sup>[10]</sup> proposed, in their pioneering study of  $Z_2$  TIs, that an uniaxial strain applied along the [111] direction to the  $\text{Pb}_x\text{Sn}_{1-x}\text{Te}$  alloy separates in energy the  $L$  point along the [111] direction from three remaining  $L$  points and may result in an odd number of band inversions (thus realizing the  $Z_2$  TI phase) at certain composition  $x$ . However, we found that such proposal will not work because  $\text{Pb}_x\text{Sn}_{1-x}\text{Te}$  alloy becomes metallic before occurring odd number of band inversions, after analyzing the band structure of  $\text{PbTe}$  and  $\text{SnTe}$  (Figure S1 in the Supplemental Material). In this Letter, we propose an alternative scheme to achieve for the first time the unusual topological phase transition between  $Z_2$  TI and TCI in a single material via atomic-ordering. We consider  $\text{PbSnTe}_2$  alloy as a prototype to demonstrate that the atomic ordering of this alloy into the CuPt phase breaks the four (parent) equivalent rocksalt  $L$  points into one (child)  $\bar{\Gamma}$  and three (child)  $\bar{F}$  points with non-identical bandgaps. Subsequently, as schematically shown in Fig. 1(a), an electrical controllable strain applied to the CuPt-ordered  $\text{PbSnTe}_2$  alloy drives gap-closing first at the child  $\bar{\Gamma}$  point (becoming odd number of band inversions) and then at the three equivalent child  $\bar{F}$  point (becoming a normal insulator), consequently, achieving a reversible quantum transition between  $Z_2$  TI and TCI phases.

The group IV chalcogenide  $\text{SnTe}$  is a prototype

TCI. It possesses a rocksalt crystal structure with  $O_h$  symmetry at room temperature, and its fundamental band gap occurs at four equivalent  $L$  points in the face-centered-cubic (FCC) Brillouin zone (BZ). Despite the fact that Sn sits between Ge and Pb in the same column of the periodic table,  $\text{SnTe}$  is a TCI with inverted bandgaps whereas  $\text{PbTe}$  and  $\text{GeTe}$  are normal trivial insulators.<sup>[26]</sup> We can easily engineer these (rocksalt) group IV chalcogenides from normal insulator to TCI or *vice versa* by forming random mixed-cation chalcogenide alloys,<sup>[27]</sup> but not from TCI to  $Z_2$  TI because the bandgaps of these alloys always occur at even (four) equivalent  $L$  points. The unusual TCI to  $Z_2$  TI topological phase transition may become possible if the alloys form lower symmetry ordered phases that break the symmetry and the equivalence of  $L$  points in rocksalt structure. Many III–V zinc-blende semiconductor alloys exhibit spontaneous CuPt-like ordering when grown epitaxially on lattice-matched substrate<sup>[28]</sup> and for IV–VI rocksalt lead chalcogenides alloys CuPt-like ordering is predicted to be the most stable phase in coherent growth.<sup>[29]</sup> To confirm this, we have calculated, using the first-principles density functional theory (DFT) (see Supplemental Material for more details of the computational method), the alloy formation energies  $\Delta H_f(\sigma, A_{1-x}B_xC) = E(\sigma, A_{1-x}B_xC) - [(1-x)E(AC) + xE(BC)]$  at composition  $x = 0.5$  (with configuration  $\sigma$  in random structure and common ordered alloy structures<sup>[29]</sup>). The ordered configurations  $\sigma$  we studied are CuPt [(1,1) superlattice along the (111) direction], CuAu [(1,1) superlattice along the (001) direction], chalcopyrite [(2,2) superlattice along the (201) direction], Y2 [(2,2) superlattice along the (110) direction], and Z2 [(2,2) superlattice along the (001) direction]. The random alloy is modeled here using the “special quasi random structures” (SQS) approach.<sup>[30]</sup> These results are summarized in Table SI in the Supplemental Material. We find that the CuPt-ordered structure with a point group of  $D_{3d}$  indeed has the lowest formation energy, indicating that rocksalt  $ABC_2$  ( $A$  or  $B = \text{Ge, Sn, Pb}$ ,  $C = \text{Te, Se}$ ) alloys can spontaneously order in the CuPt structure during lattice matched coherent growth. This finding is expected because the CuPt structure possesses the smallest strain energy over all the alloy structures because it can allow all nearest cation-anion bonds to attain their respective ideal equilibrium lengths with the minimum bond bending.<sup>[29]</sup> As a result, the energy differences between the ground state CuPt structure and the SQS structure of the  $ABC_2$  ( $A$  or  $B = \text{Ge, Sn, Pb}$ ;  $C = \text{Te, Se}$ ) alloys increase monotonically with the magnitude of the lattice mismatch between the two end constituents, as shown in Table SI. Our prediction is consistent with extensive experimental observations of CuPt-ordered structure widely in the III–V,<sup>[31–34]</sup> II–

VI,<sup>[35,36]</sup> and IV–VI<sup>[37]</sup> semiconductor alloys.

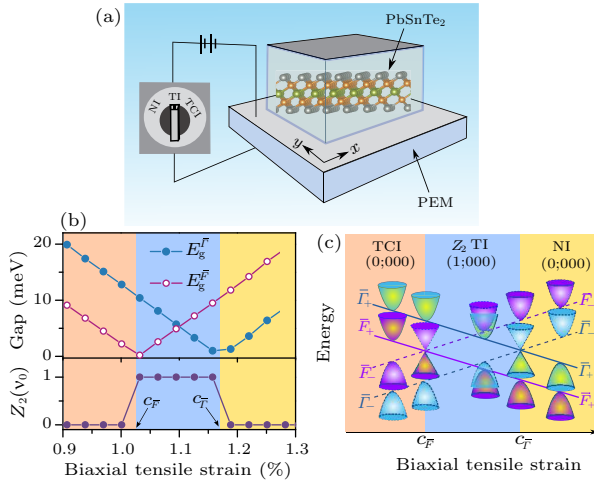


**Fig. 1.** Electrically control of reversible quantum phase transition between topological crystalline insulator (TCI) and  $Z_2$  topological insulator TI. (a) Sketch of the strain-tunable topological phase transition among topological crystalline insulator (TCI), topological insulator (TI), and normal insulator (NI). The top layer is the CuPt ordered PbSnTe<sub>2</sub> alloy. The bottom layer is the piezoelectric materials (PEM), which can change the in-plane strain by applying voltage. (b) Band gaps at  $\bar{\Gamma}$  and  $\bar{F}$  points as a function of biaxial strain, and the topological invariant quantity  $Z_2$  (here only the strong topological index  $\nu_0$  is shown for 3D system) as a function of biaxial strain for the CuPt ordered alloy. (c) The schematic evolution of band edges at  $\bar{\Gamma}$  and  $\bar{F}$  points as a function of biaxial strain (0.9%–1.3%) in the CuPt-ordered PbSnTe<sub>2</sub> alloy. The subscript (minus and plus signs) represent the odd and even parities, respectively.

The CuPt-ordered alloy structure possesses a double sized rhombohedral unit cell and thus half the BZ compared to the parent rocksalt structure, along with a symmetry reduction from  $O_h$  to  $D_{3d}$  ( $R\bar{3}m$  space group), as shown in Figs. 2(a) and 2(b). As a consequence, four equivalent  $L$  points in the rocksalt BZ transform separately to one  $\bar{\Gamma}$  point and three  $\bar{F}$  points in the reduced CuPt-like structure BZ, in which  $\bar{\Gamma}$  and  $\bar{F}$  are no longer symmetry-equivalent.<sup>[38]</sup> The bandgaps at  $\bar{\Gamma}$  and  $\bar{F}$  points may become non-identical owing to the fact that they have different symmetries, which control the inter-band coupling. Therefore, CuPt-ordered  $ABC_2$  ( $A$  or  $B = \text{Ge, Sn, Pb}$ ;  $C = \text{Te, Se}$ ) alloys provide an ideal test bed for exploring the topological phase transition from TCI to  $Z_2$  TI through engineering the band structure. If band inversion occurs only at the  $\bar{\Gamma}$  point but not at remaining TRIM  $k$  points, the CuPt-ordered alloy becomes a  $\Gamma$ -phase  $Z_2$  TI;<sup>[39]</sup> if band inversions occur exclusively at three equivalent  $\bar{F}$  points or at both  $\bar{\Gamma}$  and  $\bar{F}$  points, the alloy becomes translationally active phase TI<sup>[39]</sup> or TCI like in the SnTe, respectively. Figure S2 in the Supplemental Material shows the first-principles calculation band structure of CuPt-ordered PbSnTe<sub>2</sub> alloy with the equilibrium

lattice constant using the modified Becke and Johnson exchange potential.<sup>[40]</sup> The bandgaps at  $\bar{\Gamma}$  and  $\bar{F}$  points are indeed non-identical with values of 42.5 and 19.4 meV, respectively, although both of them are derived from the symmetry equivalent  $L$  points in the parent rocksalt group-IV tellurides. By analyzing the wave function characters, we find that the conduction band edge (CBE) at the  $\bar{\Gamma}$  point mainly comes from the anion  $p$  orbital with an even parity (+) and the valence band edge (VBE) from the cation  $p$  orbital with an odd parity (−). Such band order is same as the  $\bar{F}$  point as well as in the SnTe, indicating bandgaps at both  $\bar{\Gamma}$  and  $\bar{F}$  points are inverted and the PbSnTe<sub>2</sub> alloy is a TCI.<sup>[17]</sup> The non-identical bandgaps at  $\bar{\Gamma}$  and  $\bar{F}$  points, which are an unique property of CuPt-ordered PbSnTe<sub>2</sub> alloy, provide us an opportunity to realize the quantum phase transition from TCI to  $Z_2$  TI, considering that we could further engineer the band structure of the alloy to ensure band inversions occurring separately at  $\bar{\Gamma}$  and  $\bar{F}$  points, e.g., by applying strain or pressure.

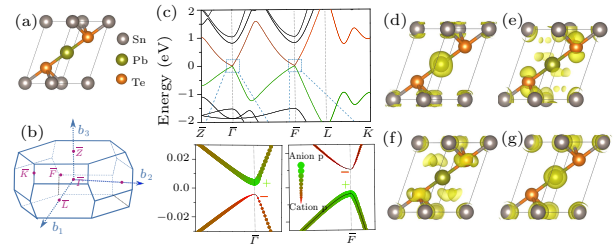


**Fig. 2.** Band structure of CuPt-order PbSnTe<sub>2</sub> alloy under biaxial strain. (a) Crystal structures of CuPt ordered PbSnTe<sub>2</sub> alloy. (b) Brillouin zone for CuPt alloy with space group  $R\bar{3}m$ . (c) Bulk band dispersions of CuPt-order PbSnTe<sub>2</sub> alloy under 1.13% tension strain are shown along high-symmetry lines  $\bar{Z}$  (0 0 0.5)– $\bar{\Gamma}$  (0 0 0)– $\bar{F}$  (0 0.5 0.5)– $\bar{L}$  (0 0.5 0)– $\bar{K}$  (0.31,0.66,0.66) calculated by the modified Becke and Johnson exchange potential. In the CuPt structure, the four equivalent  $L$  points in the rocksalt phase project into one  $\bar{\Gamma}$  and three equivalent  $\bar{F}$  points (i.e. “4=1+3”). The bottom plots show the band character of CBE and VBE near the  $\bar{\Gamma}$  and  $\bar{F}$  points, respectively. The wide green and narrow red lines indicate that the band is dominated by the anion (Te)  $p$  and cation (Sn and Pb)  $p$  states, respectively, and the corresponding parities are also labeled. (d)–(g) The charge density distribution of the VBE (d, f) and CBE (e, g) at the  $\bar{\Gamma}$ , and  $\bar{F}$  point, respectively. The value of the isosurfaces is set to  $3 \times 10^3 e/\text{\AA}^3$ .

The strain has been demonstrated to be a particular compelling tuning “knob” to engineer the electronic band structure,<sup>[18,22,41]</sup> as it can tune the interatomic lattice spacing and induce an accompanying adjustment in the electronic band structure for a fixed chemical composition. In TCIs, for example, strain has been explored to generate pseudo-magnetic fields and helical flat bands,<sup>[22]</sup> to engineer the phase transition from normal insulator to TCI,<sup>[41]</sup> and to finely modify the characteristics of the topological surface bands.<sup>[18]</sup> Controllable manipulation of strain is necessary for

the creation of suitable platforms for applications in the growing field of straintronics.<sup>[18]</sup> A promising pathway may involve the use of electric-field-induced strains,<sup>[42]</sup> in which the change of inter-atomic lattice spacing is relying on the piezoelectric response of a piezoelectric material substrate to the electric field. The piezoelectric effect is the linear electromechanical interaction between the mechanical and the electrical state in a crystal. A reversible electric-field-induced strain of over 5% has been reported, e.g., in BiFeO<sub>3</sub> films<sup>[42]</sup> and piezoelectric-induced strains have been employed, e.g., to tune semiconductor quantum dots for strain-tunable entangled-light-emitting diodes.<sup>[43]</sup> Here we propose to place the PbSnTe<sub>2</sub> alloy film onto a piezoelectric actuator via gold-thermocompression bonding, as described in Ref. [43], allowing the *in situ* application of on-demand biaxial strains by tuning the voltage (electric field), as schematically shown in Fig. 1. By sweeping the gate voltage applied to the piezoelectric actuator from negative to positive and *vice versa*, we can reversibly tune the biaxial strain applied to the PbSnTe<sub>2</sub> alloy from the compressive (negative) to the tensile (positive).

Upon application of 1.13% tensile strain, we indeed find that the CuPt-ordered TCI PbSnTe<sub>2</sub> alloy becomes a  $Z_2$  TI, achieving a novel topological phase transition from TCI to  $Z_2$  TI. Figure 2(c) shows that, at the  $\bar{\Gamma}$  point, the state of the CBE mainly comes from the anion  $p$  orbital with an even parity (+) and the state of the VBE from the cation (Pb)  $p$  orbital with an odd parity (-). Such band order is same as in the TCI SnTe and is thus inverted. However, at  $\bar{F}$  points, the state of the CBE mainly arises from the cation  $p$  orbital (-) and the state of the VBE from the anion  $p$  orbital (+), being opposite to the band order in the TCI SnTe. We assign the PbSnTe<sub>2</sub> alloy under 1.13% tensile strain as a  $\Gamma$ -phase  $Z_2$  TI because it has one band inversion (at the  $\bar{\Gamma}$  point). To further confirm our assignment, we have calculated the  $Z_2$  topological invariants (see Supplemental Material) following the procedure introduced by Soluyanov and Vanderbilt.<sup>[44]</sup> We find its  $Z_2$  being (1;000), which is an index of a strong  $Z_2$  TI,<sup>[39]</sup> despite that its end constitute SnTe is a TCI and PbTe is a trivial band insulator.

We next examine topological properties of the CuPt-ordered PbSnTe<sub>2</sub> alloy in a wide range of strains. Figure 1(b) shows the band-edge evolutions of PbSnTe<sub>2</sub> alloy as a function of biaxial strain from 0.9% to 1.3%. The CBEs at both  $\bar{\Gamma}$  and  $\bar{F}$  points shift at the same rate to lower energy, whereas VBEs to higher energy also at the same rate, as reducing the strain. Such responses of CBEs and VBEs to applied strain are expected for bonding and anti-bonding states, respectively. Because of distinct bandgaps at  $\bar{\Gamma}$  and  $\bar{F}$  points, there are two critical points  $c_{\bar{F}}$  (=1.02%) and

$c_{\bar{\Gamma}}$  (=1.16%), corresponding to the strains where band order changing occurs at  $\bar{F}$  and  $\bar{\Gamma}$  points, respectively. From band edge evolutions, we can straightforwardly find that, when strain is smaller than  $c_{\bar{\Gamma}}$  (left area in Fig. 1(b)), band inversions occur at both  $\bar{\Gamma}$  and  $\bar{F}$  points in the PbSeTe<sub>2</sub> alloy, which remains a TCI being  $Z_2$  trivial (i.e.,  $Z_2 = (0;000)$ ) but Mirror Chern number nontrivial. As we continuously increase the applied tensile strain to exceed  $c_{\bar{F}}$  but smaller than  $c_{\bar{\Gamma}}$  (middle area in Fig. 1(b)), band order changes to normal at  $\bar{F}$  points but remains inverted at the  $\bar{\Gamma}$  point, therefore PbSeTe<sub>2</sub> alloy becomes a  $Z_2$  TI (i.e.,  $Z_2 = (1;000)$ ), as shown in the bottom of Fig. 1(b). When we further increase the applied strain larger than  $c_{\bar{\Gamma}}$ , there is no band inversion occurring in PbSeTe<sub>2</sub> alloy at both  $\bar{\Gamma}$  and  $\bar{F}$  points or any other  $k$  points, indicating PbSeTe<sub>2</sub> alloy within this strain range being a trivial normal insulator (i.e.,  $Z_2 = (0;000)$ ). Therefore, we have demonstrated, for the first time, the unusual topological phase transition from TCI to  $Z_2$  TI, in addition to the quantum phase transition between normal insulator and  $Z_2$  TI. Such unusual topological transition is reversible since it is achieved with a combination of atomic ordering and strain, which can be electrically controlled by the gate electric fields via the piezoelectric effect. These transitions can be performed reversibly using the electric field to control the strain, as schematically illustrated in Fig. 1(a).

It is interesting to note that the strain can also drive the PbSnTe<sub>2</sub> alloy to become three-dimensional (3D) topological Dirac materials (TDMs), at two transition points  $c_{\bar{\Gamma}}$  (between  $Z_2$  TI and normal insulator) and  $c_{\bar{F}}$  (between  $Z_2$  TI and TCI), respectively. The 3D TDMs are another novel state of quantum matter, being viewed as a 3D graphene with linear energy dispersions along all three momentum directions rather than in a two-dimensional (2D) plane of the Dirac fermions in graphene or on the surface of 3D topological insulators. At transition point  $c_{\bar{\Gamma}}$ , PbSnTe<sub>2</sub> alloy owns a single 3D Dirac cone, whereas it possesses three 3D Dirac cones at  $c_{\bar{F}}$  point. Each 3D Dirac cone in a TDM is composed of two overlapping Weyl fermions,<sup>[45–47]</sup> which can be separated in the momentum space, by breaking the time reversal or inversion symmetry, to form the topological Weyl semimetal, a new topological quantum state exhibiting unique Fermi arcs on the surface.<sup>[48,49]</sup>

Having realized the transition between  $Z_2$  TI and TCI, we turn to compare the topological surface band structures between  $Z_2$  TI and TCI phases in the CuPt-ordered PbSnTe<sub>2</sub> alloy. Owing to the CuPt-ordered structure is symmetric about the {110} mirror planes, we calculate band structures of [001]-oriented slabs made of CuPt-ordered PbSnTe<sub>2</sub> alloy, which is symmetric through the {110} mirror plane, in TCI phase (Fig. 3(c), under zero strain) and  $Z_2$  TI phase

(Fig. 3(d), under tensile strain of 1.07%), respectively (see Supplemental Material for more details). For [001]-oriented slabs, the  $\bar{\Gamma}$  point in the CuPt-ordered alloy BZ remains at the projected zone center  $\bar{\Gamma}$  in the surface BZ, whereas one of the  $\bar{F}$  points projects to the point of  $(0, \mathbf{b}_2)$ , and the remaining two  $\bar{F}$  points to the  $\bar{X}$  point of  $(1/2 \mathbf{b}_1, 0)$  (where  $\mathbf{b}_1$  and  $\mathbf{b}_2$  are the reciprocal lattice vectors of the surface BZ (Fig. 3(b))). Apparently, the  $(0, \mathbf{b}_2)$  point is equivalent to the  $\bar{\Gamma}$  point since they are just different by a reciprocal vector of the surface BZ. Consequently, in the TCI phase, there are two Dirac cones centered at the  $\bar{\Gamma}$  point of the surface BZ as a result of the band inversions occurring at both  $\bar{\Gamma}$  and  $\bar{F}$  points. Whereas in the  $Z_2$  TI phase, there is only one Dirac cone centered at the  $\bar{\Gamma}$  point because the band inversion exists exclusively at the  $\bar{\Gamma}$  point. We therefore expect to see significant differences in the surface band structures between TCI and  $Z_2$  TI phases even in the same CuPt-ordered PbSnTe<sub>2</sub> alloy.

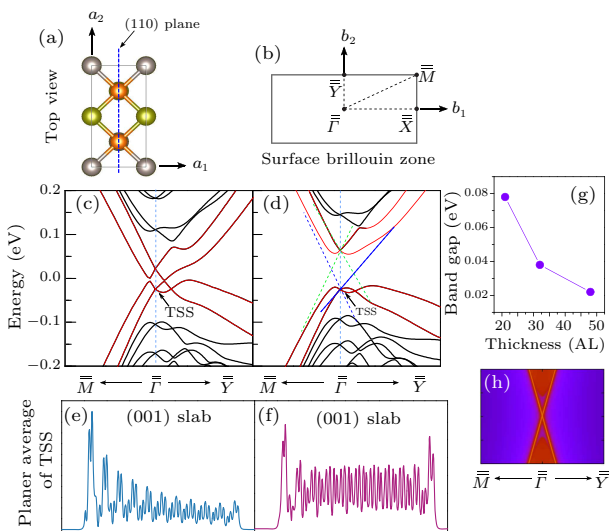


**Fig. 3.** Topological surface band structures of a 21-atomic-layer thick slab of the CuPt-ordered PbSnTe<sub>2</sub> alloy in the TCI and TI phases, respectively. (a) Crystal structure (top view) of the 21-atomic-layer thick slab made of the CuPt-ordered PbSnTe<sub>2</sub> alloy along the [001] direction. A blue dashed line indicates the (110) mirror plane. (b) The 2D surface BZ of the slab. A double overline is used to mark the high symmetry  $k$  points in the surface BZ, distinguishing from ones in reduced 3D alloy BZ (marked with single overline) and ones in the parent rocksalt BZ. (c) The topological surface band structure of the slab in the TCI phase. (d) The topological surface band structure of the slab in the TI phase. (e, f) The wavefunctions of topological surface states located at zone center for TCI and TI phases as indicated by arrows in (c) and (d), respectively. (g) The magnitude of the topological bandgap in the  $Z_2$  phase as a function of slab thickness. (h) The  $k \cdot p$  Hamiltonian model predicted Dirac cone on the surface of the semi-infinite PbSnTe<sub>2</sub> alloy in the TI phase.

Figure 3(c) shows that the predicted surface band structure of a 21 atomic layers (ALs) thick PbSnTe<sub>2</sub>

alloy slab in the TCI phase is rather complex and involves multiple Dirac cones, as expected for TCIs.<sup>[13]</sup> It consists of two parent Dirac cones centered at the  $\bar{\Gamma}$  point and vertically offset in energy owing to symmetry enforced coupling between these two Dirac cones. When they come together away from the  $\bar{\Gamma}$  point, the coupling between the lower half of the upper parent Dirac cone and the upper half of the lower parent Dirac cone opens a gap at all points except along the mirror line, leading to the formation of a pair of offspring Dirac points shifted away from the  $\bar{\Gamma}$  point. In the slab surface BZ, the  $\bar{\Gamma}$ - $\bar{Y}$  line is a mirror line, which is along the {110} reflection axis. The mirror Chern number is invariant under reflection about the {110} reflection axis, except for the  $k$ -points on the  $\bar{\Gamma}$ - $\bar{Y}$  line (Fig. 3(b)). Thus, all of the  $k$ -points off the  $\bar{\Gamma}$ - $\bar{Y}$  line have the same mirror symmetry and present the same mirror eigenvalues, whereas the  $k$ -points on the  $\bar{\Gamma}$ - $\bar{Y}$  line hold the opposite mirror eigenvalues.<sup>[13,16]</sup> Consequently, the interaction between the two parent Dirac cones is forbidden along the  $\bar{\Gamma}$ - $\bar{Y}$  direction and crosses each other, and such interaction is allowed along remaining  $k$ -points and opens a gap, leading to the formation of a pair of offspring Dirac cones. This surface band structure is consistent with that of the prototype TCI SnTe, which was discovered theoretically<sup>[13,16,22]</sup> and confirmed experimentally,<sup>[14,27]</sup> in the vicinity of Dirac points, except for two striking distinctions. Specifically, we find here that the parent Dirac cones center at the BZ center rather than those at the BZ boundary, and hence, in compared with the TCI SnTe, there is only one pair of offspring Dirac cones instead of two pairs. These two distinctions are consequences of band inversions occurring at different TRIMs in CuPt-ordered PbSnTe<sub>2</sub> alloy and SnTe, respectively. Accompanying the formation of offspring Dirac cones, more striking features could also be found in the surface band structure of the TCI phase, such as recently revealed the existence of a Lifshitz transition as a result of switching of the orbital characters of the upper parent Dirac cone and the lower parent Dirac cone.<sup>[20]</sup> The saddle point in the TCI surface band structure (along the  $k$ -line perpendicular to the mirror line away from the  $\bar{\Gamma}$  point, as shown in Fig. 3(c)) is known as the Van Hove singularity (VHS).<sup>[23]</sup> The existence of both Lifshitz transitions and VHSs provides the possibility of achieving future quantum applications.<sup>[23]</sup>

Figure 3(d) shows the corresponding surface band structure in the  $Z_2$  TI phase. In compared with a complex band structure involving multiple Dirac cones in the TCI phase, the surface band structure in the  $Z_2$  TI phase is quite simple. In general, we expect the Dirac cones centered exactly at the  $\bar{\Gamma}$  point in the  $Z_2$  TI, owing to the fact that the TRS protects

the topological states, and subsequently, without off-spring Dirac cones and absence of the Lifshitz transition points. However, we observe a finite Dirac gap of about 0.08 eV as a result of strong hybridization between the two topological surface states (TSSs) located on the top and bottom surfaces, respectively. Figure 3(g) shows, as is expected, that the magnitude of the surface bandgap decreases monotonically as the thickness of the slab increases. Such surface bandgap is an intrinsic feature of finite thick slabs and films,<sup>[50]</sup> and was frequently observed in thin films of prototype 3D chalcogenide TIs.<sup>[51,52]</sup> In order to mimic the surface states of the semi-infinite slabs, we also calculate the surface band structure based on the surface Green function with a low-energy effective  $k$ -Hamiltonian model (see the Supplemental Material for more details). We find that there is a gapless Dirac cone at the  $\bar{\Gamma}$  point formed by the surface states in the semi-infinite slab of the PbSnTe<sub>2</sub> alloy, as shown in Fig. 3(h).

In summary, we have shown that the effect of CuPt-like atomic ordering, which is expected to reduce the even number of equivalent  $L$  points into odd ones, can be used to realize the odd number of band inversions in the BZ, thus inducing a robust TCI to  $Z_2$  TI phase transition in materials such as PbSnTe<sub>2</sub>. We further show that in isovalent rocksalt alloys, the CuPt-ordered structure has the lowest alloy formation energies compared to other ordered or disordered alloys, thus can form spontaneously under coherent growth, which is consistent with extensive experimental observations of CuPt-ordered structure widely in the III–V, II–VI and IV–VI semiconductor alloys. By calculating the  $Z_2$  invariant and topological surface states, we demonstrate that the topological phase transitions from TCI to TI to normal insulator can be achieved by controlling the strain in combination with the ordering in PbSnTe<sub>2</sub>. Because this concept is also applicable to other material systems, our results suggest that atomic ordering provides a new platform to realize the quantum phase transition between different topological phases.

## References

- [1] Kane C L and Mele E J 2005 *Phys. Rev. Lett.* **95** 146802
- [2] Bernevig B A, Hughes T L and Zhang S C 2006 *Science* **314** 1757
- [3] König M et al 2007 *Science* **318** 766
- [4] Chen Y L et al 2009 *Science* **325** 178
- [5] Zhang H, Liu C X, Qi X L, Dai X, Fang Z and Zhang S C 2009 *Nat. Phys.* **5** 438
- [6] Qi X L and Zhang S C 2010 *Phys. Today* **63** 33
- [7] Hasan M Z and Kane C L 2010 *Rev. Mod. Phys.* **82** 3045
- [8] Qi X L and Zhang S C 2011 *Rev. Mod. Phys.* **83** 1057
- [9] Moore J E 2010 *Nature* **464** 194
- [10] Fu L and Kane C L 2007 *Phys. Rev. B* **76** 045302
- [11] Yang G, Liu J, Fu L, Duan W and Liu C 2014 *Phys. Rev. B* **89** 085312
- [12] Fu L 2011 *Phys. Rev. Lett.* **106** 106802
- [13] Hsieh T H, Lin H, Liu J, Duan W, Bansil A and Fu L 2012 *Nat. Commun.* **3** 982
- [14] Tanaka Y et al 2012 *Nat. Phys.* **8** 800
- [15] Dziawa P et al 2012 *Nat. Mater.* **11** 1023
- [16] Liu J, Duan W and Fu L 2013 *Phys. Rev. B* **88** 241303
- [17] Xu S Y et al 2012 *Nat. Commun.* **3** 1192
- [18] Zeljkovic I et al 2015 *Nat. Nano* **10** 849
- [19] Cao Y et al 2013 *Nat. Phys.* **9** 499
- [20] Zeljkovic I et al 2014 *Nat. Phys.* **10** 572
- [21] Luo J W and Zunger A 2010 *Phys. Rev. Lett.* **105** 176805
- [22] Tang E and Fu L 2014 *Nat. Phys.* **10** 964
- [23] Okada Y et al 2013 *Science* **341** 1496
- [24] Zeljkovic I et al 2015 *Nat. Mater.* **14** 318
- [25] Tanaka Y et al 2013 *Phys. Rev. B* **87** 155105
- [26] Ye Z Y, Deng H X, Wu H Z, Li S S, Wei S H and Luo J W 2015 *npj Comput. Mater.* **1** 15001
- [27] Yan C et al 2014 *Phys. Rev. Lett.* **112** 186801
- [28] Mascarenhas A 2001 *Spontaneous Ordering in Semiconductor Alloys* (New York: Plenum)
- [29] Wei S H and Zunger A 1997 *Phys. Rev. B* **55** 13605
- [30] Zunger A, Wei S H, Ferreira L G and Bernard J E 1990 *Phys. Rev. Lett.* **65** 353
- [31] Kondow M, Kakibayashi H, Tanaka T and Minagawa S 1989 *Phys. Rev. Lett.* **63** 884
- [32] Stringfellow G B and Chen G S 1991 *J. Vac. Sci. Technol. B* **9** 2182
- [33] Kurtz S R, Dawson L R, Biefeld R M, Follstaedt D M and Doyle B L 1992 *Phys. Rev. B* **46** 1909
- [34] Jen H R, Ma K Y and Stringfellow G B 1989 *Appl. Phys. Lett.* **54** 1154
- [35] Kim T W et al 2001 *Appl. Phys. Lett.* **78** 922
- [36] Lee H S et al 2002 *J. Appl. Phys.* **91** 5657
- [37] Schröder T et al 2011 *Phys. Rev. B* **84** 184104
- [38] Wei S H, Franceschetti A and Zunger A 1995 *Phys. Rev. B* **51** 13097
- [39] Slager R J, Mesaros A, Juricic V and Zaanen J 2013 *Nat. Phys.* **9** 98
- [40] Tran F and Blaha P 2009 *Phys. Rev. Lett.* **102** 226401
- [41] Barone P, Sante D D and Picozzi S 2013 *Phys. Status Solidi RRL* **7** 1102
- [42] Zhang J X et al 2011 *Nat. Nano* **6** 98
- [43] Zhang J et al 2015 *Nat. Commun.* **6** 10067
- [44] Soluyanov A A and Vanderbilt D 2011 *Phys. Rev. B* **83** 235401
- [45] Wang Z et al 2012 *Phys. Rev. B* **85** 195320
- [46] Liu Z K et al 2014 *Science* **343** 864
- [47] Neupane M et al 2014 *Nat. Commun.* **5** 4786
- [48] Weng H, Fang C, Fang Z, Bernevig B A and Dai X 2015 *Phys. Rev. X* **5** 011029
- [49] Xu S Y et al 2015 *Science* **349** 613
- [50] Tarasenko S A et al 2015 *Phys. Rev. B* **91** 081302
- [51] Zhang Y et al 2010 *Nat. Phys.* **6** 584
- [52] Förster T, Krüger P and Rohlfing M 2016 *Phys. Rev. B* **93** 205442

# Supplemental Material: Atomic-Ordering-Induced Quantum Phase Transition between Topological Crystalline Insulator and $Z_2$ Topological Insulator

Hui-Xiong Deng(邓惠雄)<sup>1,2,\*</sup> Zhi-Gang Song(宋志刚)<sup>1</sup> Shu-Shen Li(李树深)<sup>1,2,3</sup> Su-Huai Wei(魏苏淮)<sup>4,†</sup> and Jun-Wei Luo(骆军委)<sup>1,2,3,‡</sup>

<sup>1</sup>State Key Laboratory of Superlattices and Microstructures, Institute of Semiconductors, Chinese Academy of Sciences, P. O. Box 912, Beijing 100083, China

<sup>2</sup>University of Chinese Academy of Sciences, Beijing 100049, China

<sup>3</sup>Beijing Academy of Quantum Information Sciences, Beijing 100193, China

<sup>4</sup>Beijing Computational Science Research Center, Beijing 100094, China

## I. BAND-EDGE EVOLUTIONS OF SnTe AND PbTe AS A FUNCTION OF UNIAXIAL STRAIN ALONG [111] DIRECTION.

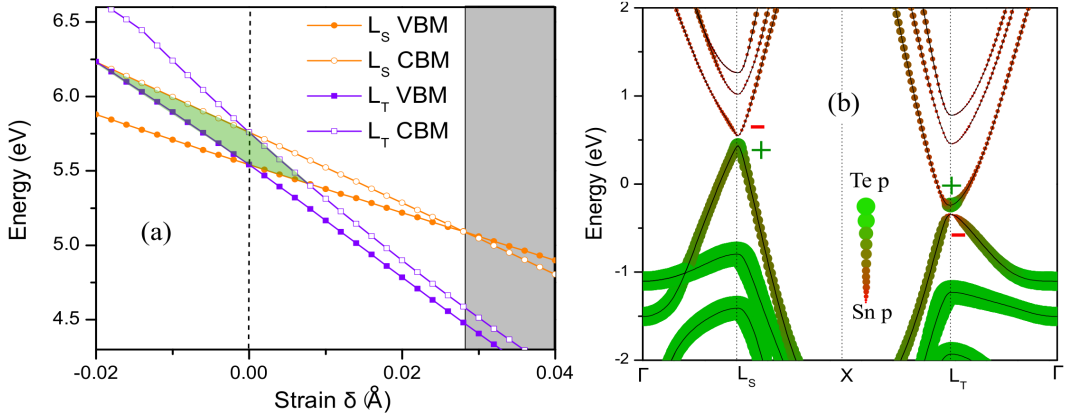


FIG. 1. (Color online) The evolutions of band-edges as function of [111] uniaxial strain. **a.** The band-edge evolutions of SnTe at the  $L$  (0.5,0.5,0.5) valley (labeled as  $L_S$ ) and remaining three equivalent  $L$  valleys (labeled as  $L_T$ ) as a function of uniaxial strain  $\delta$  along [111] direction. In the green shadow area the SnTe is a insulator with a gap, and in the gray shadow area there is a odd number of band inversion (i.e.,  $L_S$  point is back to normal band order, and the  $L_T$  point is still inverted). **b.** Band structure of SnTe with the application of the [111]-oriented uniaxial strain  $\delta=0.042$ . The wide green and narrow red lines indicate the band is dominated the Te  $p$  and Sn  $p$  states, respectively, and corresponding parities are also labeled.

Fu et al.[1] proposed in their pioneering study of  $Z_2$  TIs that an uniaxial strain along the [111] direction could lift the equivalence of four  $L$  points in the  $\text{Pb}_{1-x}\text{Sn}_x\text{Te}$  alloy, leading to the bandgap at the  $L$  point along the [111] direction (labeled as  $L_S$ ) different from that of remaining three equivalent  $L$  points (labeled as  $L_T$ ). They therefore postulated that the strained  $\text{Pb}_{1-x}\text{Sn}_x\text{Te}$  alloy might have odd number of band inversion at certain composition and become a  $Z_2$  TI. Here, we have assessed this idea in detail in terms of examining the band-edge evolutions of the end constitute SnTe as a function of uniaxial strain along the [111] direction by performing first-principles calculations. Fig. 1 shows that the equivalence of four  $L$  points in the rocksalt structure is indeed broken and band-edges at the

\* hxdeng@semi.ac.cn

† suhuaiwei@csrc.ac.cn

‡ jwluo@semi.ac.cn

$L_S$  point shift away from that of remaining three equivalent  $L_T$  points once an uniaxial strain is applied along the [111] direction with their energy deviations being proportional to strain strength  $\delta$ . However, it is almost impossible to find a case having simultaneously a global bandgap and odd times of band inversions. We find that the bandgap deformation at the  $L_S$  point is much larger than that at the  $L_T$  point, which enables us to drive bandgap at the  $L_S$  back to normal order leaving behind bandgap at remaining three  $L_T$  points keeping inverted. But, deformation potentials of both conduction band valence band-edges at the  $L_T$  point are so negative that before driving  $L_S$ -valley band gap back to normal order the uniaxial strain already moves the  $L_T$  bandgap fully out the  $L_S$  bandgap leading to vanishing of global bandgap and SnTe become metallic, as shown in Fig.1(b). The gray shadow area in Fig.1(a) indicates the global bandgap of strained SnTe. Although we archive the odd number of band inversion after the transition of the bandgap order at the  $L_S$  point to normal, the transition point is too way from the shadow area, leading to the conduction band edge at the  $L_T$  valley is lower in energy than the valence band edge at the  $L_S$  point and strained SnTe becomes a metallic, as shown in the Fig. 1(b) for the band structure of SnTe with  $\delta=0.042$ . We have verified that this fact is also true for PbTe that when odd number of band inversions occurs, it is no longer a insulator.

## II. IDENTIFY THE GROUND CRYSTAL STRUCTURE OF ROCKSALT $A_xB_{1-x}C$ ALLOYS.

To determine the ground crystal structure of rocksalt  $A_xB_{1-x}C$  (A or B=Ge, Sn, Pb, C=Te, Se) alloys, we have calculated the alloy formation energies  $\Delta H_f(\sigma, A_xB_{1-x}C)$  at composition  $x = 0.5$  for most commonly observed alloy configurations  $\sigma$  [2], which include ordered CuPt, CuAu, chalcopyrite, Y2, and Z2 structures as well as a random alloy described using the ‘‘special quasi random structures’’ (SQS) approach[3]. The predicted results using first-principles calculations are summarized in Table S1. We found unambiguously that in all investigated systems, the CuPt ordered configuration has the lowest formation energy among all examined configurations, owing to CuPt-ordered structure allows all nearest cation-anion bond lengths to attain their respective equilibrium lattice with the minimum bond bending and holds the smallest strain energy among all studied configurations [2].

TABLE I. Calculated formation energies (unit in meV/4-atom) of rocksalt  $A_xB_{1-x}C$  (A or B=Ge, Sn, Pb, C=Te, Se) alloys at composition  $x = 0.5$  with varying configurations of ordered CuPt, CuAu, chalcopyrite, Y2, and Z2 structures as well as a SQS random alloy structure.

systems	CuPt	CuAu	Y2	Z2	CH	SQS
$\text{Sn}_{0.5}\text{Pb}_{0.5}\text{Te}$	11	21	15	17	17	12
$\text{Sn}_{0.5}\text{Pb}_{0.5}\text{Se}$	11	19	15	15	14	13
$\text{Ge}_{0.5}\text{Sn}_{0.5}\text{Te}$	18	116	49	81	75	45
$\text{Ge}_{0.5}\text{Sn}_{0.5}\text{Se}$	40	157	74	106	102	69
$\text{Ge}_{0.5}\text{Pb}_{0.5}\text{Te}$	58	256	111	169	170	100
$\text{Ge}_{0.5}\text{Pb}_{0.5}\text{Se}$	98	329	153	217	218	137
$\text{GeSe}_{0.5}\text{Te}_{0.5}$	19	129	54	80	85	52
$\text{SnSe}_{0.5}\text{Te}_{0.5}$	20	142	60	85	93	49
$\text{PbSe}_{0.5}\text{Te}_{0.5}$	23	145	78	94	93	54

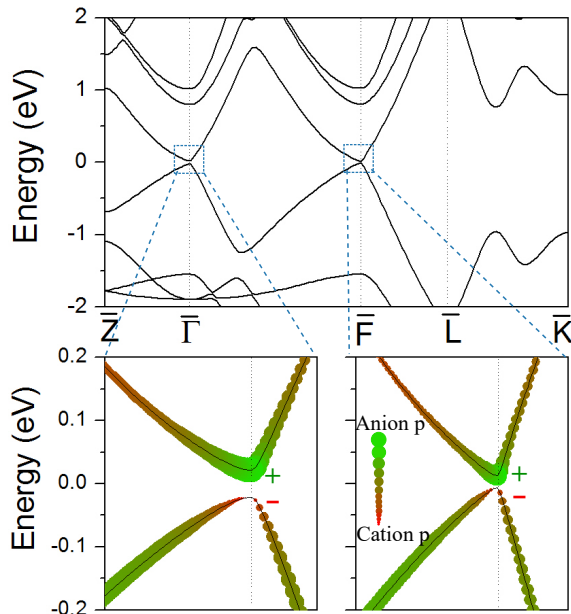


FIG. 2. (Color online) Band structure of CuPt-ordered PbSnTe<sub>2</sub> alloy under the equilibrium lattice constant. The wide green and narrow red lines indicate the band dominated by the anion (Te)  $p$  and cation (Sn and Pb)  $p$  orbitals, respectively. The parity symmetry is also labeled.

### III. BAND STRUCTURE OF CuPt-ORDERED PbSnTe<sub>2</sub> ALLOY UNDER THE EQUILIBRIUM LATTICE CONSTANT.

Figure 2 shows the band structure of CuPt-ordered PbSnTe<sub>2</sub> alloy under the equilibrium lattice constant. Along with the transform of equivalent four  $L$  points in parent PbTe and SnTe to one  $\bar{\Gamma}$  and three  $\bar{F}$  points in CuPt-ordered PbSnTe<sub>2</sub> alloy, energy gaps at the  $\bar{\Gamma}$  and  $\bar{F}$  points are now different remarkably, which is caused by inter-band coupling as a result of symmetry reduction from (rocksalt)  $O_h$  to (CuPt-type structure)  $D_{3d}$ . After analyzing the characters of band-edge wave functions, we found that the conduction band edges at both  $\bar{\Gamma}$  and  $\bar{F}$  points, mainly comes from the anion  $p$  orbit with an even parity (“+”), and the valence band edges from the cation  $p$  orbit with an odd parity (“-”), illustrating the bandgaps at both  $\bar{\Gamma}$  and  $\bar{F}$  points being inverted and hence the PbSnTe<sub>2</sub> alloy being a TCI under equilibrium condition.

### IV. CALCULATIONS OF TOPOLOGICAL INVARIANT $Z_2$ .

The  $Z_2$  index in 2D systems is a single invariant, but in 3D system is a complex of four invariants, i.e.,  $Z_2=(\nu_0; \nu_1\nu_2\nu_3)$ , where  $\nu_0$  is the strong topological index and  $\nu_1, \nu_2$ , and  $\nu_3$  are three weak indices ( $\nu_0 = 1$  alone indicates a strong topological insulator without inquiring  $\nu_1\nu_2\nu_3$ ;  $\nu_0 = 0$  is a weak topological insulator if at least one of  $\nu_1, \nu_2, \nu_3$  equal to 1). Only the strong topological insulator ( $\nu_0=1$ ), which is named as a  $Z_2$  TI, has robust topological surface states protected by time-reversal symmetry and against weak disorders. According to the time-reversal polarization theory developed by Fu and Kane[4], the integer  $Z_2$  invariant of a time-reversal ( $\mathcal{T}$ ) symmetric system can be written as  $\Delta = P_\theta(T/2) - P_\theta(0) \text{ mod } 2$ , where  $P_\theta$  is defined as the “time-reversal polarization”. Later, Soluyanov and Vanderbilt [5] further simplified this method by utilizing Wannier functions as a basis set, and implemented it within the *ab initio* plan-wave calculations. They suggested that we can simply calculate the  $Z_2$  invariant by tracking the spectrum of Wannier charge centers (WCCs)  $\bar{\chi}_n$  and determining the center of the largest gap  $z^m$  between two adjacent WCCs

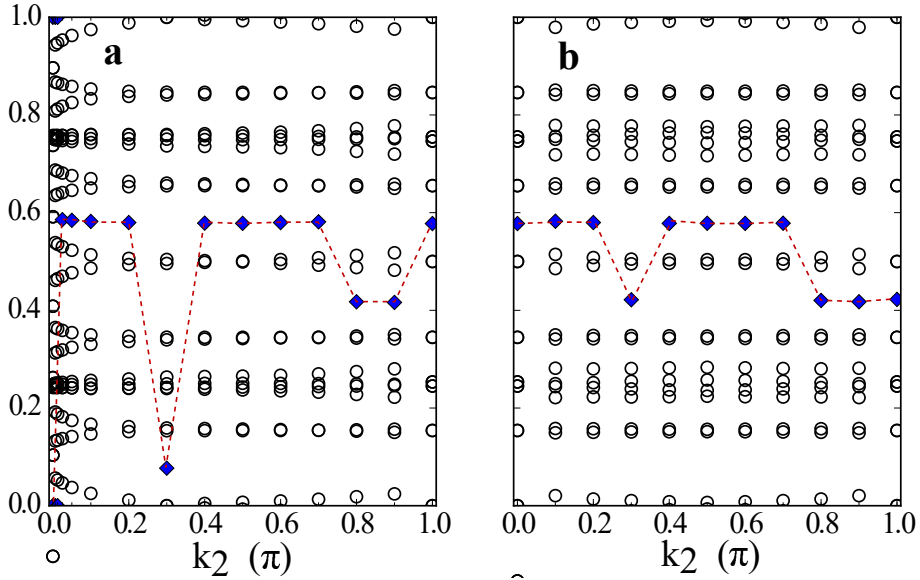


FIG. 3. (Color online) Evolution of WCCs  $\bar{\chi}_n$  of CuPt ordered  $\text{Sn}_{0.5}\text{Pb}_{0.5}\text{Te}$  alloy in the  $r_3$  direction vs  $k_2$  at (a)  $n_1=0$ ; (b)  $n_1=1$ . Blue rhombus indicates the midpoint of largest gap.  $k_2$  is sampled in 14 increments from 0 to  $\pi$ . From this figure, it is seen that for the  $n_1=0$  surface it has a odd number of jumps of the  $\bar{\chi}_n$ , so the  $\nu_0 = 1$ , and for  $n_1=1$  surface has a even number of jumps of the  $\bar{\chi}_n$ , so the  $\nu_1 = 0$ . Furthermore, the  $R\bar{3}m$  symmetry in the CuPt structure guarantees the  $\nu_1=\nu_2=\nu_3=0$ . Thus, the  $Z_2 = (1:000)$ .

on the circle. The overall  $Z_2$  invariant can then be obtained as,

$$\Delta = \sum_{m=0} \Delta_m \text{ mod } 2 \quad . \quad (1)$$

$$(-1)^{\Delta_m} = \prod_{n=1}^{\mathcal{N}} \text{sgn}[g(2\pi z^m, 2\pi z^{m+1}, 2\pi \bar{\chi}_n^{m+1})]$$

where  $\text{sgn}(x)$  is the sign function, and  $g(\phi_1, \phi_2, \phi_3) = \sin(\phi_2 - \phi_1) + \sin(\phi_3 - \phi_2) + \sin(\phi_1 - \phi_3)$ , which is the directed area of a triangle defined by angles  $\phi_1, \phi_2, \phi_3$  on a unit circle.  $\mathcal{N}$  is the number of occupied bands. For more details about these method, please refer to the Fu and Soluyanov's papers[4, 5].

Due to the CuPt-ordered  $\text{Sn}_{0.5}\text{Pb}_{0.5}\text{Te}$  alloy has a  $R\bar{3}m$  symmetry, which has a threefold rotational axis leading to  $\nu_1=\nu_2=\nu_3$ , one only needs to calculate one weak  $Z_2$  index  $\nu_1$ , i.e.  $n_1=1$  surface of the parallelepiped constructed by the eight time-reversal points in the reciprocal space. Similarly, one only needs to calculate one more of the  $Z_2$  invariants for  $n_1=0$  surface to get the strong topological index  $\nu_0$ . Figure 3 shows the calculated evolution of WCCs  $\bar{\chi}_n$  of CuPt-ordered  $\text{Sn}_{0.5}\text{Pb}_{0.5}\text{Te}$  alloy upon application of 1.13% tensile strain in the  $r_3$  direction vs  $k_2$  at (a)  $n_1=0$  (i.e.  $k_1=0$ ); (b)  $n_1=1$  (i.e.  $k_1=\pi$ ). We found that for the  $n_1=0$  surface, the gap center jumps over 11 WCCs near the  $k_2=0$ , and over 10 WCCs at  $k_2=0.2$  and  $k_2=0.3$ , and then over 2 WCCs at  $k_2=0.7$  and  $k_2=0.9$ , respectively. Thus, the total number of jumps is  $11+10+10+2+2=35$ , an odd number. For the  $n_1=1$  surface, similarly, we get a total of  $2+2+2=6$  jumps, which is even number. In terms of the Eq. (1), we obtain  $\nu_0 = 1$ , and  $\nu_1 = \nu_2 = \nu_3 = 0$  ( $Z_2 = (1:000)$ ), and hence CuPt-ordered  $\text{Sn}_{0.5}\text{Pb}_{0.5}\text{Te}$  alloy upon application of 1.13% tensile strain is a strong  $Z_2$  TI.

## V. EFFECTIVE HAMILTONIAN MODEL FOR CALCULATING TOPOLOGICAL SURFACE STATES AT $Z_2$ TI PHASE.

We can use the model Hamiltonian method to simulate semi-infinite slabs. Most of  $Z_2$  TIs such as  $\text{Bi}_2\text{Se}_3$ ,  $\text{Bi}_2\text{Te}_3$ ,  $\text{Sb}_2\text{Te}_3$  as well as  $\text{Sn}_{0.5}\text{Pb}_{0.5}\text{Te}$  alloy in  $Z_2$  phase the band inversions occur at the  $\Gamma$  point, we are able to calculate the topological surface band structure using a simple low-energy effective Hamiltonian  $H_\Gamma(k)$  near the  $\Gamma$  point [6]. The symmetry of  $\Gamma$  point in CuPt-ordered  $\text{Sn}_{0.5}\text{Pb}_{0.5}\text{Te}$  alloy belongs to the space group  $D_{3d}$  which is same as in  $\text{Bi}_2\text{Se}_3$ , the low-energy effective Hamiltonian  $H_\Gamma(k)$  near  $\Gamma$  point for CuPt-ordered  $\text{PbSnTe}_2$  alloy is therefore written as [6],

$$H_\Gamma(\mathbf{k}) = \epsilon_0(\mathbf{k}) \mathbf{I}_{4 \times 4} + \begin{pmatrix} M(\mathbf{k}) & A_1 k_z & 0 & A_2 k_- \\ A_1 k_z & -M(\mathbf{k}) & A_2 k_- & 0 \\ 0 & A_2 k_+ & M(\mathbf{k}) & -A_1 k_z \\ A_2 k_+ & 0 & -A_1 k_z & -M(\mathbf{k}) \end{pmatrix} \quad (2)$$

where  $k_\parallel^2 = k_x^2 + k_y^2$ ,  $k_\pm = k_x \pm ik_y$ .  $\epsilon_0(k) = C + D_1 k_z^2 + D_2 k_\parallel^2$  and  $M(k) = m - B_1 k_z^2 - B_2 k_\parallel^2$ . All of these parameters in the effective model can be obtained by fitting the energy spectrum of the effective Hamiltonian with that of the first-principles calculations.

In order to explore surface states of the semi-infinite slabs, we calculate the surface Green Function (GF) according to Refs.[7, 8]. Here a simple description about the process is shown. The equation of Green Function of the semi-infinite slabs is following:

$$\begin{pmatrix} \epsilon - H_s & H_{SR} \\ H_{SR}^\dagger & \epsilon - H_R \end{pmatrix} \begin{pmatrix} G_s & G_{SR} \\ G_{RS} & G_R \end{pmatrix} = \mathbf{I} \quad (3)$$

where  $H_S$  is a  $N \times N$  matrix which represents the hamiltonian of surface and  $H_R$  is a  $\infty \times \infty$  matrix which represents the bulk. Both of them can be constructed through the effective hamiltonian by introducing  $k_i \rightarrow \frac{1}{R_i} \sin(k_i R_i)$  and  $k_i^2 \rightarrow \frac{2}{R_i^2} [1 - \cos(k_i R_i)]$ . The Eq.(3) can be written in another format:

$$\begin{cases} G_s = (\epsilon - H_s - \Sigma_R)^{-1} \\ \Sigma_R = H_{SR} g_R H_{SR}^\dagger \\ g_R = (\epsilon - H_R)^{-1} \end{cases} \quad (4)$$

where  $\Sigma_R$  denotes the self-energy induced by  $H_R$  and  $G_S$  denotes the surface green function. As the  $H_R$  is a  $\infty \times \infty$  matrix, which cannot be directly solved, we utilize the iteration numerical method to solve above equation. Dividing the  $H_R$  into two parts  $H_R \rightarrow H_{R_0} + H_{R'}$ , we can write similar equations as Eq.(3):

$$\begin{pmatrix} \epsilon - H_{R_0} & H_{R_0 R'} \\ H_{R_0 R'}^\dagger & \epsilon - H_{R'} \end{pmatrix} \begin{pmatrix} g_{R_0} & g_{R_0 R'} \\ g_{R' R_0} & g_{R'} \end{pmatrix} = \mathbf{I} \quad (5)$$

In addition, the nearest layer hopping along the slab direction will add some limitation:

$$H_{SR} = \begin{pmatrix} H_{SR_0} \\ H_{SR'} \end{pmatrix} \approx \begin{pmatrix} H_{SR_0} \\ 0 \end{pmatrix} \quad (6)$$

Thus, the self-energy part can be given as:

$$\Sigma_R = H_{SR} g_R H_{SR}^\dagger = \begin{pmatrix} H_{SR_0} & 0 \end{pmatrix} \begin{pmatrix} g_{R_0} & g_{R_0 R'} \\ g_{R' R_0} & g_{R'} \end{pmatrix} \begin{pmatrix} H_{SR_0} \\ 0 \end{pmatrix} = H_{SR_0} g_{R_0} H_{SR_0}^\dagger \quad (7)$$

Now, having transformed an  $\infty \times \infty$  problem into a  $N \times N$  problem, we need to obtain the  $g_{R_0}$ . The  $g_R$  green function is

$$\begin{pmatrix} \epsilon - H_{R_0} & -H_{R_0, R_1} & 0 & \cdots \\ -H_{R_0, R_1}^\dagger & \epsilon - H_{R_0} & -H_{R_0, R_1} & \cdots \\ 0 & -H_{R_0, R_1}^\dagger & \epsilon - H_{R_0} & \cdots \\ \vdots & \vdots & \vdots & \ddots \end{pmatrix} \begin{pmatrix} g_{R_0} & g_{R_0, R_1} & g_{R_0, R_2} & \cdots \\ g_{R_1, R_0} & g_{R_0} & g_{R_1, R_2} & \cdots \\ g_{R_2, R_0} & g_{R_2, R_1} & g_{R_0} & \cdots \\ \vdots & \vdots & \vdots & \ddots \end{pmatrix} = \mathbf{I} \quad (8)$$

We can write above as the linear format:

$$\begin{cases} (\epsilon - H_{R_0}) g_{R_0} = \mathbf{I} + H_{R_0, R_1} g_{R_1, R_0} \\ (\epsilon - H_{R_0}) g_{R_1, R_0} = H_{R_0, R_1}^\dagger g_{R_0} + H_{R_0, R_1} g_{R_2, R_0} \\ \vdots \\ (\epsilon - H_{R_0}) g_{R_n, R_0} = H_{R_0, R_1}^\dagger g_{R_{n-1}, R_0} + H_{R_0, R_1} g_{R_{n+1}, R_0} \end{cases} \quad (9)$$

By defining

$$\begin{cases} t_0 = (\epsilon - H_{R_0})^{-1} H_{R_0, R_1}^\dagger \\ \tilde{t}_0 = (\epsilon - H_{R_0})^{-1} H_{R_0, R_1} \\ t_i = (\mathbf{I} - t_{i-1} \tilde{t}_{i-1} - \tilde{t}_{i-1} t_{i-1})^{-1} t_{i-1}^2 \\ \tilde{t}_i = (\mathbf{I} - t_{i-1} \tilde{t}_{i-1} - \tilde{t}_{i-1} t_{i-1})^{-1} \tilde{t}_{i-1}^2 \end{cases} \quad (10)$$

Eq.(9) can be transformed into

$$\begin{cases} g_{R_1, R_0} = t_0 g_{R_0} + \tilde{t}_0 g_{R_2, R_0} \\ g_{R_2, R_0} = t_1 g_{R_0} + \tilde{t}_1 g_{R_2, R_0} \\ \vdots \\ g_{R_{2n}, R_0} = t_n g_{R_0} + \tilde{t}_n g_{R_{2n+1}, R_0} \\ \vdots \end{cases} \quad (11)$$

When  $n \rightarrow \infty$ ,  $t_n \tilde{t}_n$  will tend to 0 and the  $g_{R_{2n}, R_0}$  also will tend to 0. we need to do a truncation.

$$\begin{aligned} g_{R_1, R_0} &= t_0 g_{R_0} + \tilde{t}_0 g_{R_2, R_0} \\ &= t_0 g_{R_0} + \tilde{t}_0 t_1 g_{R_0} + \tilde{t}_1 g_{R_2, R_0} \\ &\quad \dots \\ &= (t_0 + \tilde{t}_0 t_1 + \tilde{t}_0 \tilde{t}_1 t_2 + \cdots + \tilde{t}_0 \tilde{t}_1 \cdots t_N) g_{R_0} + \tilde{t}_1 \tilde{t}_2 \cdots \tilde{t}_N g_{R_{2N}, R_0} \\ &\approx T g_{R_0} \end{aligned}$$

where

$$T = (t_0 + \tilde{t}_0 t_1 + \tilde{t}_0 \tilde{t}_1 t_2 + \cdots + \tilde{t}_0 \tilde{t}_1 \cdots t_N) \quad (12)$$

Take above into Eq.(9) we can get

$$g_{R_0} = (\epsilon - H_{R_0} - H_{R_0, R_1} T)^{-1} \quad (13)$$

Finally, we obtain the semi-infinite system green function

$$\begin{cases} G_s = (\epsilon - H_s - \Sigma_R)^{-1} \\ \Sigma_R = H_{SR_0} g_{R_0} H_{SR_0}^\dagger \\ g_{R_0} = (\epsilon - H_{R_0} - H_{R_0, R_1} T)^{-1} \end{cases} \quad (14)$$

Therefore, the local densities of states can be obtained:

$$N(\mathbf{k}_{||}, \epsilon + i\eta) = -\frac{1}{\pi} \text{Im} \sum_{\alpha} G_s^{\alpha, \alpha}(\mathbf{k}_{||}, \epsilon + i\eta) \quad (15)$$

Based on above method, we have calculated the topological surface structure of CuPt-ordered  $\text{Sn}_{0.5}\text{Pb}_{0.5}\text{Te}$  alloy in  $Z_2$  phase, as shown in Fig. 3h in main text.

## VI. DETAILS OF FIRST-PRINCIPLES COMPUTATIONAL METHOD.

To engineer the band structure of alloys, we perform the first-principles calculations using the frozen-core projector-augmented wave method (PAW) within the density functional theory (DFT)[9, 10] and generalized-gradient-approximation (GGA) to the exchange-correlation potential as implemented in the VASP code[11–13]. We have carefully examined the convergence of the plane-wave cutoff energy and the Monkhorst-Pack k-point mesh. In all calculations, all the atoms are allowed to relax until the quantum mechanical forces acting on them become less than 0.02 eV/Å. The spin-orbit coupling (SOC) term is included. Regarding semi-local exchange-correlation functionals, such as GGA, usually remarkably underestimate the bandgaps of semiconductors[14], as a comparison, we have also employed the modified Becke and Johnson exchange potential (hereafter called TB-MBJ), which has the comparable accuracy with the hybrid functional and GW method, but much less computational cost[15]. For example, the TB-MBJ calculated normal gap of PbTe and inverted gap of SnTe are 0.20 eV and -0.19 eV, respectively, very close to experimental values. The random alloys are mimicked by the special quasirandom structures (SQS)[3, 16].

Different from model Hamiltonian method to calculate the topological surface band structure, in the atomistic first-principles approach we are free from the need to judge at the outset which selected 3D bulk bands will couple in surface. We do so by solving the surface band structure using explicitly the microscopic potential of a slab constructed by  $\text{SnPbTe}_2$  alloy along the (001) direction, in which the slab nanostructure is viewed as a system in its own right rather than express it in terms of a preselected basis drawn from its bulk parent bands. The slab having e.g., 21 atomic layers, is sandwiched between 20 Å thick vacuum layers along the (001) direction. Since one slab has unavoidable two pristine surfaces (i.e., top and bottom surfaces), there always exist two Dirac cones: one on the top surface and another on the bottom surface. The symmetry of the 2D slabs enforces these two Dirac cones coupling each other, opening a topological Dirac gap. Attempt to reduce this coupling effect by splitting two Dirac cones in energy, we use the pseudo-Hydrogen (PH) to passivate the dangling bonds on top surface and leave behind the dangling bonds on the bottom surface unpassivated. However, at  $Z_2$  TI phase, we still observe a finite Dirac gap, which is almost vanished at TCI phase. As shown in Fig. 3 in the main text, the magnitude of the Dirac gap drops remarkably as expected, owing to reduced coupling between two surface Dirac cones as increasing the slab thickness. Such surface bandgap is an intrinsic feature of finite slabs and films, and is frequently observed in thin films of prototype 3D chalcogenide TIs.

---

[1] Fu L and Kane C L 2007 Phys. Rev. B **76** 045302

[2] Wei S H and Zunger A 1997 Phys. Rev. B **55** 13605

- [3] Zunger A, Wei S H, Ferreira L G and Bernard J E 1990 Phys. Rev. Lett. **65** 353
- [4] Fu L and Kane C L 2006 Phys. Rev. B **74** 195312
- [5] Soluyanov A A and Vanderbilt D 2011 Phys. Rev. B **83** 235401
- [6] Zhang H, Liu C X, Qi X L, Dai X, Fang Z and Zhang S C 2009 Nat. Phys. **5** 438
- [7] Sancho M P L, Sancho J M L and Rubio J 1984 Journal of Physics F: Metal Physics **14** 1205
- [8] Sancho M P L, Sancho J M L and Rubio J 1985 Journal of Physics F: Metal Physics **15** 851
- [9] Kohn W and Sham L J 1965 Phys. Rev. **140** A1133
- [10] Hohenberg P and Kohn W 1964 Phys. Rev. **136** B864
- [11] Kresse G and Hafner J 1993 Phys. Rev. B **47** 558
- [12] Kresse G and Hafner J 1993 Phys. Rev. B **48** 13115
- [13] Kresse G and Furthmuller J 1996 Comput. Mater. Sci. **6** 15
- [14] Perdew J P and Levy M 1983 Phys. Rev. Lett. **51** 1884
- [15] Tran F and Blaha P 2009 Phys. Rev. Lett. **102** 226401
- [16] Wei S H, Ferreira L G, Bernard J E and Zunger A 1990 Phys. Rev. B **42** 9622